Finite Element Analysis of the Microstructure of AlN-TiN Composites

Satyanarayan Patel, Rahul Vaish*, Niraj Sinha and C. R. Bowen
School of Engineering, Indian Institute of Technology Mandi, Himachal Pradesh 175 001, India

*Email: rahul@iitmandi.ac.in Phone: +91-1905-237921, Fax: +91-1905-237924

Abstract

Finite element modelling (FEM) has been performed on AlN-TiN composites. The structure-property relationships are studied for 5vol.% and 10vol.% TiN composites in view of thermal and thermo-mechanical properties. Thermal stresses are simulated at various temperatures for the 5% and 10% TiN samples in homogeneous and heterogeneous temperature environments. It is found that compressive stresses created are associated with the microstructure and these stresses are largest at the interface of the AlN-TiN phases. In addition, thermal strains are simulated at various temperatures for both the compositions. Thermal conductivity and thermal expansion coefficient are estimated using FEM and compared with other known analytical methods.

Keywords: AlN-TiN; Object Oriented Finite Element Analysis; Thermal Conductivity; Thermal Expansion; Thermal Stresses

1. INTRODUCTION

Aluminum nitride (AlN) has been extensively used in thermal coatings where high electrical resistivity ($1\times10^{13}\ \Omega.m$), high thermal conductivity (160 $W/m.K$), low dielectric constant (9 at 300 K) and high corrosion resistance are required [1-3]. It is also an attractive material for other applications such as seals, semiconductor devices, grinding media, transducers and electronic substrates [4,5]. AlN is a brittle material and it exhibits poor mechanical properties in context of fracture toughness and flexural strength [6]. Therefore, it is difficult to be use in structural applications [7]. A number of additive materials such as titanium carbide (TiC), titanium nitride (TiN), and zirconium (Zr) are used to increase the fracture toughness and flexural strength of AlN based materials [8]. These composites have been extensively studied for their possible applications in microelectronic devices, protective coatings for cutting tools, corrosion resistance, tribology and other mechanical devices [9,10].

In recent years, AlN-TiN composites have gained increasing attention because of their superior thermo-mechanical properties from both practical and theoretical viewpoints [6]. It exhibits a wide range of electrical resistivity, thermal conductivity and fracture toughness which can be controlled by the microstructure and composition [6]. A number of analytical and numerical methods are available for estimation of physical properties of composite materials [11-16].

A novel numerical approach called object-oriented finite element technique (OOF2) has been developed by National Institute of Standards and Technology (NIST), which is used for finite element modeling (FEM) of microstructural images from optical and electron microscopy [15]. In this method a two-dimensional (2-D) microstructural (10^{-6}-10^{2} m) image can be used for the analysis. It has been previously used by many researchers in examining residual thermal stress [17,18], thermal conductivity [19] and crack propagation mechanism [20,21] of composite materials. The present study deals with FEM analysis of AlN-TiN composites. In this context, microstructural images of AlN-TiN composites are used to simulate thermal and thermo-mechanical behavior of these composites at various temperatures.

2. Finite Element Modelling

The finite element code of OOF2 (http://www.ctcms.nist.gov/oof/oof2/) version 2.1.7 can be used for the analysis of mechanical, thermal, pyroelectric and piezoelectric properties of materials. It can be directly applied to the microstructural images of materials to determine their effective properties. The main advantage of this method is that the real image of the microstructure of a material can contain the particle size, shape and spatial orientation of specific phases which can be combined with its physical and mechanical properties (such as

thermal conductivity, thermal expansion coefficient, Young's modulus, Poisson's ratio, and piezoelectric coefficient) to predict the overall behavior of a material. However, this method is currently limited to 2-D microstructural modelling [16].

The first step of the analysis involves importing a scanning electron microscopy (SEM) microstructure image of a multiphase material (in this case AlN-TiN). Two different types of microstructure images of AlN-TiN composites having 5% and 10% by volume TiN are used in present study as shown in Figure 1 [5]. This experiment has been performed by Masahiko Tajika *et al.* [5]. The SEM images indicate the presence of some porosity, which is less in 10% TiN composition as compared to 5% TiN composition. The representative volume element (RVE) size of both the compositions is same at 55 by 64 μm. In these figures black, gray, and white colors represent AlN, TiN and pores, respectively. Common segmentation methods such as blur filters, contrast, despeckle, sharpness, normalize, reduce noise and threshold adjustments are used to regulate the image quality. These segmentation methods are very important for effective microstructural modeling. The next step is single phase material selection and assignment of their properties. Single phase material pixels are selected according to their colors as shown in Figure 1. After selectingthe single phase material, their mechanical (Young's modulus and Poisson's ratio) and thermal (thermal conductivity and thermal expansion coefficient) properties are assigned. The mechanical and thermal properties for AlN and TiN used in this work are listed in Table 1.

2.1. Mesh generation

Mesh generation is the next step after assigning material properties. The mesh is generated on the microstructure using skeletons. The skeleton is defined as "the geometry of the mesh only; it does not include any field, equations and shape function" [23]. The skeleton is generated on the microstructure and then refined. The skeleton refinement process depends on minimization of energy functional parameter (*En*) of the elements, which in turn depends on homogeneity energy (En_h) and shape energy (En_s). The homogeneity energy of elements is defined as [24]:

$$En_h = 1 - En_{hm} \quad (1)$$

where En_{hm} is the homogeneity energy of the microstructure elements. The homogeneity energy is minimized when elements are completely homogeneous. Shape energy for triangular and quadrilateral elements is as [15]:

$$En_s = 1 - 4\sqrt{3}\frac{A_T}{L^2} \quad (2)$$

$$En_s = 1 - [(1-\gamma).Q_m + \gamma.Q_o] \quad (3)$$

where A_T is the area of the triangular element and L is the side length of triangle, Q_m is the minimum Q_i in element and Q_o is the Q_i at the opposite corner.The factor γ is required to prevent pathologies, which occur when shape energy of element does not depend on the position of one of the nodes. The shape energy is zero for equilateral triangular element and has a value of one when aspect ratio is zero (all the vertices are collinear) [24]. For quadrilateral elements, the shape energy is found by first computing a "quality factor", Q_i, for each corner i. Q_i is the area of the parallelogram "which can be defined by two sides of the element that converge at node i, divided by the sum of the squares of the sides" [23]. Its value is always less than one at a corner where the two converging edges have different lengths or meet at an acute or obtuse angle. The value of Q_i is zero in the degenerate cases when the edges are collinear or when the length of one edge is zero.

The sum of these two energy components En_h and En_s gives the energy functional parameter (En), which is given as [15]:

$$En = \theta En_h + (1-\theta)En_s \qquad (4)$$

where θ is a parameter whose value varies from 0 to 1. It can be inferred from Eq. (4) that when θ = 0, only the shape energy of the element gives the total modification energy of the elements. Similarly, then the shape energy of the elements do not contribute in total modification energy when θ = 1. The shape energy En_s and homogeneous energy En_h are shown in Figure 2. This figure contains three types of elements. For element 1, both shape energy and homogeneous energy are zero ($En_s = En_h = 0$) because the element is a perfect shape (assumed as equilateral triangle) and homogenous. For element 2, the shape energy is zero but the homogeneous energy is not zero. This is due to the fact that it contains more than one material. Similarly, the homogeneous energy is for element 3 but the shape energy is not zero. This is because the element is degenerate.

The mesh size depends on the homogeneity, which is controlled by initial skeleton size. For this purpose many skeleton refinement processes (skeleton modifier) are used for minimization of the energy functional parameter such as snap refine, merge triangle, snap node, swap edge, rationalize and smooth. These skeleton modifier processes are applied on the microstructure image. Modifier tools can be used for refining only interface elements without affecting whole microstructure elements. On the base of skeleton elements, a finite element mesh is generated and the final mesh is shown in the Figure 3. Boundary conditions are applied on the mesh after selection of field and equations. Pore areas are selected in the

microstructure and deactivated andindicate that such pixels will not play any role in final results as they have not assigned any physical properties.

2.2 Fundamental assumptions

In the present study, it is assumed that AlN-TiN composites are linearly elastic and isotropic. Mechanical and thermal properties of the AlN and TiN are considered as homogenous in the individual phases. It is assumed that the composites have perfect bonding between their interfacial surfaces. Since the analsysis is a 2-D finite element mesh simulation it neglects the effect of thickness. It is assumed during material's pixel selection that some particles of AlN or TiN material are present in middle of the pores. They are considered as pores since particles that are present in pores cannot define their degree of freedom during the simulation. Materials properties are assumed to be constant in the temperature range understudy.

3. Results and discussions

3.1 Thermal stress analysis

In order to study the local thermal stresses, 2-D simulations are performed on the above-mentioned composites. Thermal stresses are estimated for both the composites containing 5% and 10% TiN under different temperature environments. Thermal stresses can be calculated as:

$$\sigma = E.\alpha.\Delta T \qquad (5)$$

where σ is thermal stress, ε is the thermal strain, α is coefficient of thermal expansion, E is Young's modulus and ΔT is change in the temperature. Thermal stresses in this study are estimated in the following two conditions: (i) uniform temperature environment, and (ii) temperature gradient environment.

3.1.1 Uniform temperature environment

The uniform temperature is applied on the image and thermal stresses are estimated in the composites. A typical image of uniaxial stress contour (σ_{xx}) at 600 $°C$ of AlN-TiN (5% TiN) is shown Figure 4. A similar type of stress contours are plotted for different temperatures and compositions (not shown in the figure). Stress contours are plotted for σ_{xy} and σ_{xy} however the σ_{xx} H stress contour of is discussed here since it shows highest stresses. It is observed that the stresses are highest at the sharp edges/interfaces of the TiN and AlN phases. The TiN phase has high stress intensity region because of its larger CTE than that of the matrix (see Table 1). It is interesting to note that the stresses vary from one filler region to other region and are non-uniform in an individual filler region. The stress distribution is dependent on the

particle size [18]. Plastic deformation of material can occurr when local stresses exceed the yield strength of the matrix (AlN) [17].

In order to further study the thermal stress distribution at phase interfaces, we have performed a line scan in stress contour. The stress variation along the line (shown in Figure 4) is shown in Figure 5. Tensile and compressive stresses are observed in the matrix and filler, respectively. There are sharp transitions (from tensile to compressive) at the interfaces between TiN and AlN. Intensity of stresses (compressive in nature) is highest at the interfaces as compared to that of filler and matrix.

Thermal stresses are estimated at various temperatures for both the compositions under study. Figure 6 shows upper and lower limits of thermal stresses generated in the composites. It is found that local thermal stresses increase linearly with temperature. These stresses are also increase with TiN content. It is due to the fact that the number of interfaces increase with an increase in the volume fraction of filler material [18]. Compressive stresses are generated in most of the microstructure region. It is to be noted that while AlN based materials can be used for high temperature applications up to 750 $°C$ (oxidization temperature of AlN*)* [47] it is observed here than for uniform temperature applications the thermal stresses exceeds the yield strength (2.1 GPa) of the matrix below the oxidization temperature that results in a lowering of the working temperature.

The thermal strain (ε_{xx}) contour for 5% TiN composites is shown in Figure 7. Thermal strains are larger at the interfaces as compared to matrix and filler phases, since the interfaces are associated with highest local stresses. It is to be noted that the TiN has higher Young's modulus than that of AlN (Table 1); therefore the thermal strain in the filler is less compared to the strain in the matrix phase. Some regions in the filler have very high thermal strain as shown in the inset of Figure 6 and areresponsible for higher stress generation. These strain regions can be deleterious to the mechanical properties of the composites.

3.1.2 Temperature gradient environment

In order to further analyze the thermal stress behavior, simulations are performed under heterogeneous temperature environment as shown in Figure 8. The 2-D simulations are performed under various temperature gradients (ΔT) while other two boundaries are kept adiabatically insulated. Upper and lower bounds of local thermal stresses are estimated at 0-800$°C$ temperature gradient as shown in Figure 8. It is observed that the magnitude of stresses increase as the temperature increases. These stress distributions are attributed to the morphology, distribution and orientation of filler material [16]. The magnitude of

compressive stresses associated with filler materials largely depend upon their orientation. Insets A and B of Figure 8 show two different orientations of filler material in same temperature zone. It is found that the stresses are larger when the particles are orientated in the direction of temperature gradient (inset A, Figure 8) as compared to transverse particles (inset B, Figure 8). This implies that thermal stresses can be tailored using different alignments of filler material in the composites. The localized higher thermal stress around the filler increase the likelyhood of plastic deformation as discussed in previous sections. In summary, the thermal stress depends on the reinforcement size, misfit strain, elastic modulus and matrix toughness [17].

Thermal stresses are estimated when different temperature gradients are applied on the boundaries of the microstructural models. The resultant upper and lower limits of thermal stresses are shown in Figure 9 for both the compositions under study. It is observed that the stresses vary with the variation in the filler material and temperature gradient as discussed in previous sections. The intensity of stresses is found to be lower than that of stresses generated in uniform temperature environment. The thermal strain distribution in 5% TiN composites is shown in Figure 10 at a temperature gradient of 0 $^{\circ}C$ -800 $^{\circ}C$. It varies from left side edge to right side edge due to variation in temperature (temperature gradient). The strain distribution increases in matrix and filler material linearly. The filler has higher strain as compared to the matrix and this can be attributed to its larger CTE than that of the matrix (Table 1).

3.2 Thermal conductivity

The mode of heat transfer in these ceramics is only via phonons which can be scattered by defects. Thermal conductivity is highly sensitive to grain size, porosity, orientation of secondary phase and other defects. In this section the thermal conductivity of the composites has been estimated using OOF2 code and calculated using a temperature gradient on the image boundaries and solved using the steady state heat equation. In this study, thermal conductivities are calculated at a temperature gradient of 10 $^{\circ}C$. For this purpose left and right vertical edges are kept at 25 $^{\circ}C$ and 35 $^{\circ}C$ temperatures, respectively as shown in Figure 11, while the top and bottom edges are perfectly insulated (Figure 11). It is seen that the heat flux varies in composites due to difference in thermal conductivities of materials as well as the presence of pores. The thermal conductivity of the composites (κ_c) can be calculated as [19]:

$$\kappa_c = \frac{Q_{avg}}{dT/dx} \qquad (6)$$

where Q_{avg} is the average heat energy flux per unit area, dT is temperature difference, and dx is width of the microstructural image. A number of theoretical methods/models exist for the

prediction of effective thermal conductivity of composites. These models include effective-medium theory [25], parallel or series model [26], geometric mean model [27], Lewis & Nielsen [28] and Maxwell [29] methods.

The effective-medium theory (EMT) assumes that when a portion of the matrix material is replaced by one of the filler materials, the relevant fields, stress, strain, electric field and thermal field change in the whole composites [25]. Through the Laplace equation for heat transfer, the EMT equation for thermal conductivity is derived and can be expressed as:

$$V_m \frac{\kappa_m - \kappa_c}{\kappa_m + 2\kappa_c} + V_f \frac{\kappa_f - \kappa_c}{\kappa_f + 2\kappa_c} = 0 \qquad (7)$$

where κ is thermal conductivity and V denotes volume fraction. The subscripts c, f, and m refer to the composites, filler and matrix respectively. Another simple alternative method for two phase composites assumes that the composite materials are arranged either in parallel or in series with respect to the heat flow [26]. In this work, the average of parallel and series thermal conductivity values is used for calculation. The parallel conduction model is given as:

$$\kappa_c = V_m \kappa_m + V_f \kappa_f \qquad (8)$$

The series conduction model can be written as:

$$\frac{1}{\kappa_c} = \frac{V_m}{\kappa_m} + \frac{V_f}{\kappa_f} \qquad (9)$$

Further, effective thermal conductivity of the composites is determined by geometric mean model (GMM) and is given by [27]:

$$\kappa_c = \kappa_m^{V_m} . \kappa_f^{f} \qquad (10)$$

Furthermore, Lewis and Nielsen have derived a semi-theoretical model using the Halpin-Tsai equation [28]. This method is including the effect of the shape of the filler and the orientation or type of packing for a two-phase system. The thermal conductivity of the composite can be calculated as:

$$\kappa_c = \kappa_m \frac{1 + A.\beta.V_f}{1 - \beta.V_f.\Psi} \qquad (11)$$

where

$$\beta = \frac{\frac{\kappa_f}{\kappa_m} - 1}{\frac{\kappa_f}{\kappa_m} + A} ; \qquad (12)$$

$$\Psi = 1 + \frac{1 - \Phi_m}{\Phi_m^2} V_f ; \qquad (13)$$ and

$$A = k_E - 1 \qquad (14)$$

In above-mentioned equations, A is a constant that depends upon the shape and orientation of the dispersed filler particles, k_E is Einstein constant, and Φ_m is ratio of the maximum packing fraction of the dispersed filler to the volume they appear to occupy when packed to their maximum extent. For randomly packed aggregates of spheres and irregularly shaped particles, A=3 and Φ_m=0.637 [30].

Finally, the Maxwell method is used for determining the thermal conductivity of the composite consisting of non-interacting and randomly distributed homogeneous filler in a homogeneous matrix [29]. It is expressed as:

$$\kappa_c = \kappa_m \frac{\kappa_f + 2.\kappa_m + 2.V_f.(\kappa_f - \kappa_m)}{\kappa_f + 2.\kappa_m - V_f.(\kappa_f - \kappa_m)} \qquad (15)$$

These models have been previously used by number of researchers [31-35] for estimating effective thermal conductivities at low filler concentrations. When the filler concentration is increased, they begin to touch each other and form conductive chains in the direction of heat flow (percolation). Therefore, these models underestimate the value of effective thermal conductivity in case of higher concentration of filler.

The values of thermal conductivity calculated using OOF2 and found to be 103 *W/m.K* and 120 *W/m.K* for 5% and 10% TiN respectively. The values of thermal conductivity (as calculated by other methods) are listed in Table 2. It is observed that the thermal conductivity of 10% TiN composites shows good agreement with that of thermal conductivities calculated by other methods under study. However, 5% TiN composites do not exhibit good agreement with other methods. This is due to the presence of relatively more porosity (Figure 1) which has not been considered in any of the above theories (Eq. 7-15). Porosity decreases the thermal conductivity of the composites and hence FEM predicts lower values of the thermal conductivity in the composites under study [19].

3.3 Thermal expansion coefficient

A temperature difference of 10 *°C* is applied on the boundaries of the microstructure (Figure 11) and CTE of the composites is determined by using following formula:

$$\alpha_{avg} = \varepsilon_{avg} / \Delta T_{avg} \qquad (16)$$

where α_{avg} is average coefficient of thermal expansion, ε_{avg} is the average thermal strain and ΔT_{avg} is the average temperature difference. The simulated and analytically calculated coefficients of thermal expansion have also been compared. A number of analytical models exist for the prediction of effective CTE of composites reinforced with filler. These models include simple rule of mixtures [36] and thermo-elastic energy models such as Kerner model [37], Schapery model [38], and Turner model [39].

According to the rule of mixtures, the CTE of the composite (α_c) is given by [36]:

$$\alpha_c = V_m \alpha_m + V_f \alpha_f \quad (17)$$

The Kerner model is most widely used for discontinuous, spherical and wetted reinforced filler in a uniform layer of matrix [37]. It is assumed that the composite material is macroscopically isotropic and homogeneous. This model gives the CTE of composite as:

$$\alpha_c = \alpha_f V_f + \alpha_m V_m + V_m V_f (\alpha_f - \alpha_m) \frac{(K_f - K_m)}{\alpha_f V_f + \alpha_m V_m + \frac{5}{4} K_f K_m G_m} \quad (18)$$

where K is the bulk modulus and G is the shear modulus of the composite material. K and G are related to the Young's modulus (E) and the Poisson's ratio (ν) of isotropic materials as:

$$K = \frac{E}{3(1-2\nu)} \quad (19)$$

$$G = \frac{E}{2(1+\nu)} \quad (20)$$

The Schapery model considers stress interaction between composite components and effective CTE is calculated [38]. During the calculation, an extremum principle of thermo-elasticity is used that can be illustrated as:

$$\alpha_c = \alpha_f + (\alpha_m - \alpha_f) \frac{(\frac{1}{K_c} - \frac{1}{K_f})}{(\frac{1}{K_m} - \frac{1}{K_f})} \quad (21)$$

$$K_c^+ = K_f + V_m / \left[\frac{1}{K_m - K_f} + \frac{V_f}{K_f + 4G_f/3} \right] \quad (22)$$

where K_c is the bulk modulus of the composites given by the Hashin and Shtrikman bounds [40]. This equation provides a relationship between the bulk modulus and the CTE of composites. This model assumes that the Poisson's ratio of the composites components do not differ much. It is important to note that in this model α_C depends on the volume fraction and phase geometry only through their effect on the bulk modulus. In this analysis, the CTE of the composites is determined for upper bounds (K_c^+) and lower bounds (K_c^-) bulk modulus of the composites and the average is used. The lower bound bulk modulus is determined by Eq. (22) after inter changing subscripts *f* and *m*.

Finally, the Turner model considers homogeneous strain throughout the composites. It also assumes that only uniform hydrostatic stresses exist in the phases [39]. The stresses are assumed to be sufficient to disrupt the composites. The sum of the internal forces could be equated to zero and an expression for the CTE is given by the following equation:

$$\alpha_c = \frac{\alpha_f V_f K_f + \alpha_m V_m K_m}{V_f K_f + V_m K_m} \quad (23)$$

These models have been previously applied by a number of researchers [41-45] for calculating the CTE of two-phase isotropic, particulate reinforced composites. The CTE determined by OOF2 for composites containing 5% and 10% TiN are 4.49 x 10^{-6} $°C^{-1}$ and 4.89 x 10^{-6} $°C^{-1}$ respectively. The values of CTE as calculated by method discussed above are shown in Table 3. The CTE predicted by OOF2 are in good agreement with the calculated values by these methods. FEM predicts lower values of the CTE in the present composite due to the porosity. It is observed that the CTE increases with increase in values of filler materialsonce the filler material has a higher CTE than the matrix material (Table 1). Such studies are helpful to understand material behavior for technical applications.

4. Conclusions

Finite element technique is used for study the thermal properties of AlN-TiN composites. Thermal stress distributions at various temperatures are examined for the composites (5% and 10% TiN) in homogeneous and heterogeneous temperature environments. Local thermal stresses and strains are studied on the microstructure images of these composites. The local stresses are found to be maximum at the interfaces of AlN and TiN phases. The compressive stresses (at interfaces) are found to be maximum as compared to matrix and filler regions. Thermal conductivity and coefficient of thermal expansion are estimated and compared with various theoretical models/methods.

Acknowledgment

One of the authors (Rahul Vaish) acknowledges support from the Indian National Science Academy (INSA), New Delhi, India, through a grant by the Department of Science and Technology (DST), New Delhi, under INSPIRE faculty award-2011 (ENG-01).

References

1. Fesenko, I., Kisly, P., Kuzenkova, M., Prikhna, T. and Sulzhenko, V. (2000) Properties of AlN–TiN composite ceramics. *Brit. Ceram. T.* **99**, 278-279.
2. Watari, K., Ishizaki, K. and Fujikawa, T. (1992) Thermal conduction mechanism of aluminium nitride ceramics. *J. Mater. Sci.* **27**, 2627-2630.
3. Wagner, J.M. and Bechstedt, F. (2002) Properties of strained wurtzite GaN and AlN: *ab initio* studies. *Phys. Rev. B* **66**, 115202.
4. Kida, M., Weber, L., Monachon, C. and Mortensen, A. (2011) Thermal conductivity and interfacial conductance of AlN particle reinforced metal matrix composites. *J. Appl. Phys.* **109**, 064907-064908.

5. Tajika, M., Matsubara, H. and Rafaniello, W. (1999) Microstructures and properties in aluminum nitride–titanium nitride composite ceramics. *Mater. Lett.* **41,** 139-144.
6. Tangen, I.L., Yu, Y., Grande, T., Høier, R. and Einarsrud, M.A. (2004) Preparation and characterisation of aluminium nitride–titanium nitride composites. *J. Eur. Ceram. Soc.* **24**, 2169-2179.
7. Burkhardt, S., Riedel, R. and Müller, G. (1997) Processing and properties of AlN matrix composite ceramics containing dispersed hard materials. *J. Eur. Ceram. Soc.* **17**, 3-12.
8. Senthil, K. A., Raja D. A. and Sornakumar, T. (2003) Machinability of hardened steel using alumina based ceramic cutting tools. *Int. J. Refract. Met. H.* **21**, 109-117.
9. Du, R., Okamura, H., Watanabe, R. and Kawasaki, A. (2004) Characterization of TiN-AlN composites prepared through mechanical alloying and followed by pressure sintering. *Mater. T.* **45**, 2669-2672.
10. Mosina, T., Panasyuk, A., Yuga, A. and Grigor'ev, O. (1999) Friction properties of composites of the system TiN− AlN. I. Effect of structure and phase composition of friction and wear of materials of the system TiN− AlN. *Powder Metall. Met. C*+. **38**, 517-520.
11. Garboczi, E. J. and Berryman, J. G. (2001) Elastic moduli of a material containing composite inclusions: Effective medium theory and finite element computations. *Mech. Mater.* **33**, 455-470.
12. Ayari, F., Ayari, F., Bayraktar, E. and Amar, C. B. (2012). Image processing and Finite Element modelling for analysis of a metal matrix composite. *Int. J. Comput. Sci.* ***9*****,** 448-457.
13. Qing, H. (2013) Automatic generation of 2D Micromechanical finite element model of silicon-carbide/aluminum metal matrix composites: effects of the boundary conditions. *Mater. Design,* **44**, 446-453.
14. Balasivanandha Prabu, S., and Karunamoorthy, L. (2008) Microstructure-based finite element analysis of failure prediction in particle-reinforced metal–matrix composite. *J. Mater. Process. Technol.* **207**, 53-62.
15. Chawla, N., Patel, B., Koopman, M., Chawla, K., Saha, R., Patterson, B., Fuller, E. and Langer, S. (2002) Microstructure-based simulation of thermomechanical behavior of composite materials by object-oriented finite element analysis. *Mater. Charact.* **49**, 395-407.

16. Dong, Y. and Bhattacharyya, D. (2010) Mapping the real micro/nanostructures for the prediction of elastic moduli of polypropylene/clay nanocomposites. *Polymer* **51**, 816-824.
17. Vedula, V.R., Glass, S.J., Saylor, D.M., Rohrer, G.S., Carter, W.C., Langer, S.A. and Fuller, Jr E.R. (2001) Residual-stress predictions in polycrystalline alumina. *J. Am. Ceram. Soc.* **84**, 2947-2954.
18. Cannillo, V., Leonelli, C. and Boccaccini, A.R. (2002) Numerical models for thermal residual stresses in Al< sub> 2</sub> O< sub> 3</sub> platelets/borosilicate glass matrix composites. *Mater. Sci. Eng. A* **323**, 246-250.
19. Gupta, M., Curry, N., Markocsan, N., Vaßen, R. and Nylén, P. (2013) Design of next generation thermal barrier coatings-experiments and modelling. *Surf. Coat. Technol.* **220**, 20‑26.
20. Cannillo, V., Bondioli, F., Lusvarghi, L., Montorsi, M., Avella, M., Errico, M. and Malinconico, M. (2006) Modeling of ceramic particles filled polymer–matrix nanocomposites. *Compos. Sci. Technol.* **66**, 1030-1037.
21. Michlik, P. and Berndt, C. (2006) Image-based extended finite element modeling of thermal barrier coatings. *Surf. Coat. Technol.* **201**, 2369-2380.
22. Pierson, H. O. (1996). *Handbook of Refractory Carbides & Nitrides: Properties, Characteristics, Processing and Apps*. Access Online via Elsevier.
23. S. A. Langer A.C.E.R., V. R. Coffman, G. Dogan, S. Haan, R. E. Garcia, R. C. Lua, <http://www.ctcms.nist.gov/~langer/oof2man/Section-Concepts-Skeleton.html>.
24. Reid, A.C.E., Langer, S.A., Lua, R.C., Coffman, V.R., Haan, S.I. and García, R.E. (2008) Image-based finite element mesh construction for material microstructures. *Comput. Mater. Sci.* **43**, 989-999.
25. He, H., Fu, R., Han, Y., Shen, Y. and Song, X. (2007) Thermal conductivity of ceramic particle filled polymer composites and theoretical predictions. *J. Mater. Sci.* **42**, 6749-6754.
26. Sarwar, M. and Majumdar, P. (1995) Thermal conductivity of wet composite porous media. *Heat Recov. Syst. CHP* **15**, 369-381.
27. Zhou, S., Chiang, S., Xu, J., Du, H., Li, B., Xu ,C. and Kang, F. (2012) Modeling the in-plane thermal conductivity of a graphite/polymer composite sheet with a very high content of natural flake graphite. *Carbon*. **50**, 5052-5061.

28. Lewis, T. and Nielsen, L. (1970) Dynamic mechanical properties of particulate-filled composites. *J. Appl. Polym. Sci.* **14**, 1449-1471.
29. Maxwell, J.C. (1954) *A Treatise on Electricity and Magnetism*. 3edn., Dover, New York.
30. Nielsen, L.E. (1974) The thermal and electrical conductivity of two-phase systems. *Ind. Eng. Chem. Fundam.* **13**, 17-20.
31. Chou, T.W. and Nomura, S. (1981) Fibre orientation effects on the thermoelastic properties of short-fibre composites. *Fibre Sci. Technol.* **14**, 279-291.
32. Berger, M.A. and McCullough, R.L. (1985) Characterization and analysis of the electrical properties of a metal-filled polymer. *Compos. Sci. Technol.* **22**, 81-106.
33. Tavman, I. (1998) Effective thermal conductivity of isotropic polymer composites. *Int. Commun. Heat Mass* **25**, 723-732.
34. Shojaei, A., Fahimian, M. and Derakhshandeh, B. (2007) Thermally conductive rubber-based composite friction materials for railroad brakes–Thermal conduction characteristics. *Compos. Sci. Technol.* **67**, 2665-2674.
35. Kaundal, R., Patnaik, A. and Satapathy, A. (2012) Comparison of the Mechanical and Thermo-Mechanical Properties of Unfilled and SiC Filled Short Glass Polyester Composites. *Silicon* **4**, 175-188.
36. Zhao, L., Zhao, M., Cao, X., Tian, C., Hu, W. and Zhang, J. (2007) Thermal expansion of a novel hybrid SiC foam–SiC particles–Al composites. *Compos. Sci. Technolo.* **67**, 3404-3408.
37. Kerner, E. (2002) The elastic and thermo-elastic properties of composite media. *Proc. phys. Soc. London Sect. B* **69**, 808.
38. Schapery, R.A. (1968) Thermal expansion coefficients of composite materials based on energy principles. *J. Compos. Mater.* **2**, 380-404.
39. Turner, P.S. (1946) Thermal-expansion stresses in reinforced plastics. *J. Res. Nat. Stand.* **37**.
40. Hashin, Z. and Shtrikman, S. (1963) A variational approach to the theory of the elastic behaviour of multiphase materials. *J. Mech. Phys. Solids* **11**, 127-140.
41. Wegner, L. and Gibson, L. (2000) The mechanical behaviour of interpenetrating phase composites–I: modelling. *Int. J. Mech. Sci.* **42**, 925-942.
42. Fei, W. and Wang, L. (2004) Thermal expansion behavior and thermal mismatch stress of aluminum matrix composite reinforced by β-eucryptite particle and aluminum borate whisker. *Mater. Chem. Phys.* **85**, 450-457.

43. Nam, T.H., Requena, G. and Degischer, P. (2008) Thermal expansion behaviour of aluminum matrix composites with densely packed SiC particles. *Composites Part A* **39**, 856-865.

44. Wu, G. and Zhu, D. (2009) Thermal expansion and mechanical properties of high reinforcement content SiCp/Cu composites fabricated by squeeze casting technology. *Transactions of Nonferrous Metals Society of China* **19**, 600-604.

45. Mizuuchi, K., Inoue, K., Agari, Y., Nagaoka, T., Sugioka, M., Tanaka, M., Takeuchi, T., Tani, J., Kawahara, M. and Makino, Y. (2012) Processing and thermal properties of Al/AlN composites in continuous solid–liquid co-existent state by spark plasma sintering. *Composites Part B* **43**, 1557-1563.

46. Tien, S. K., and Duh, J. G. (2006). Comparison of microstructure and phase transformation for nanolayered CrN/AlN and TiN/AlN coatings at elevated temperatures in air environment. *Thin Solid Films*, **515,** 1097-1101.

Figure captions

Table 1: Mechanical and thermal properties of AlN and TiN materials.

	Young's modulus (*GPa*)	**Poisson's ratio**	**Thermal expansion coefficient($^oC^{-1}$)**	**Thermal conductivity (*W/m.K*)**
AlN	322[3]	0.21[3]	4.6 x 10^{-6}[6]	160[2]
TiN	477[12]	0.21[12]	9.1 x 10^{-6}[6]	20[22]

Table 2: Estimation of thermal conductivity using various methods

Method	Thermal conductivity (κ_c) *W/m.K*	
	5% TiN	10% TiN
OOF2	103	120
Effective-medium theory	150	143
Parallel or series model	135	120
Geometric mean model	144	129
Lewis and Nielsen	151	142
Maxwell	150	141

Table 3: Estimation of CTE using various methods

Method	Coefficient of thermal expansion α_c x 10^{-6} $^oC^{-1}$	
	5 % TiN	10% TiN
OOF2	4.49	4.89
Rule of mixture	4.82	5.05
Kerner	4.83	5.05
Schapery	4.90	5.15
Turner	4.93	5.24

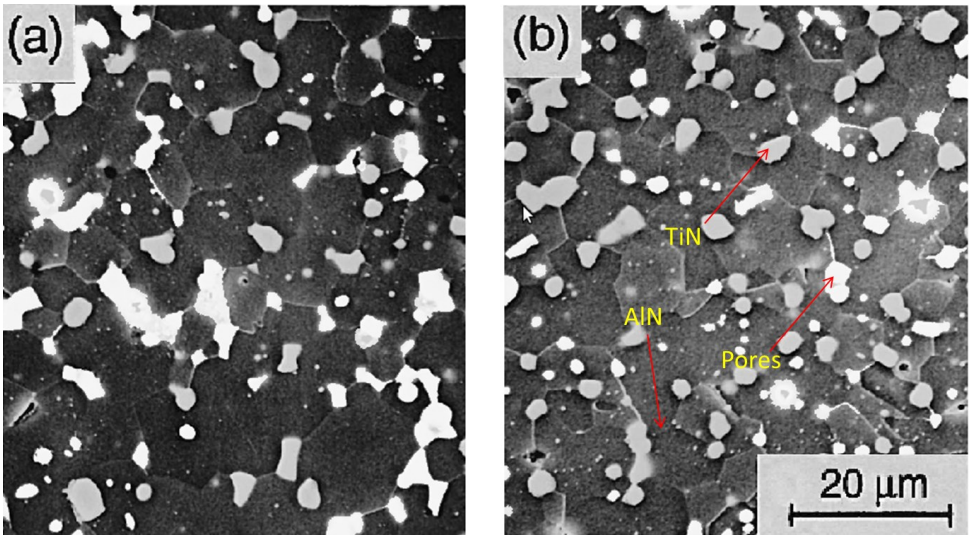

Figure 1:

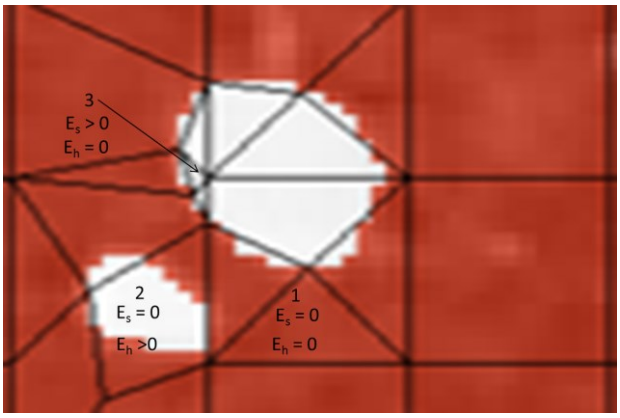

Figure 2:

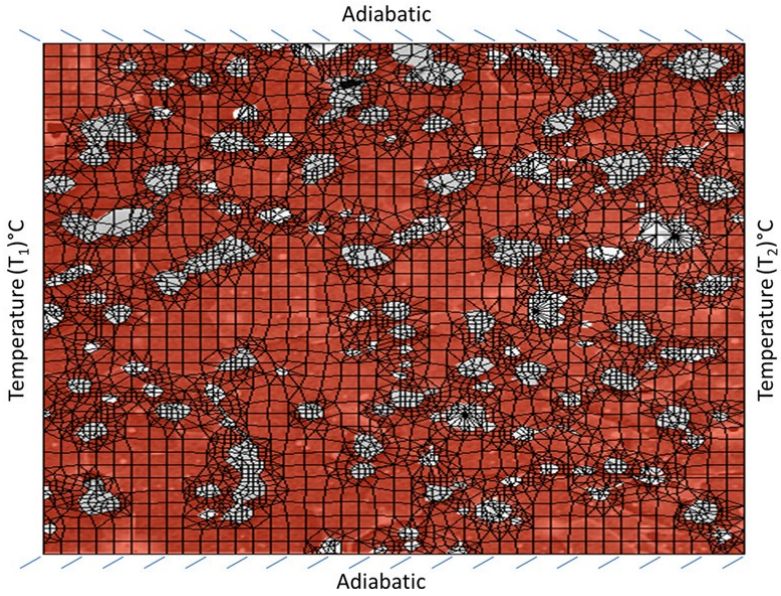

Figure 3:

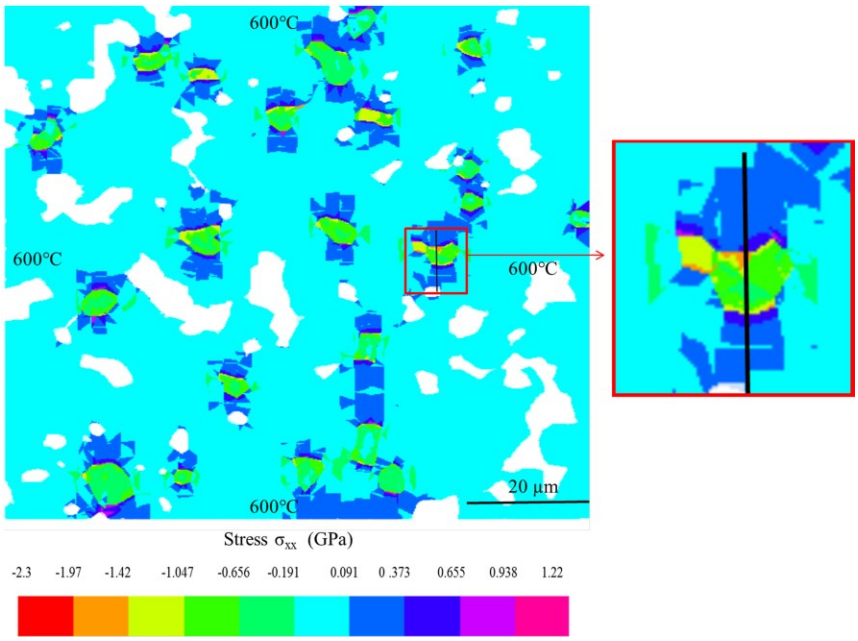

Figure 4:

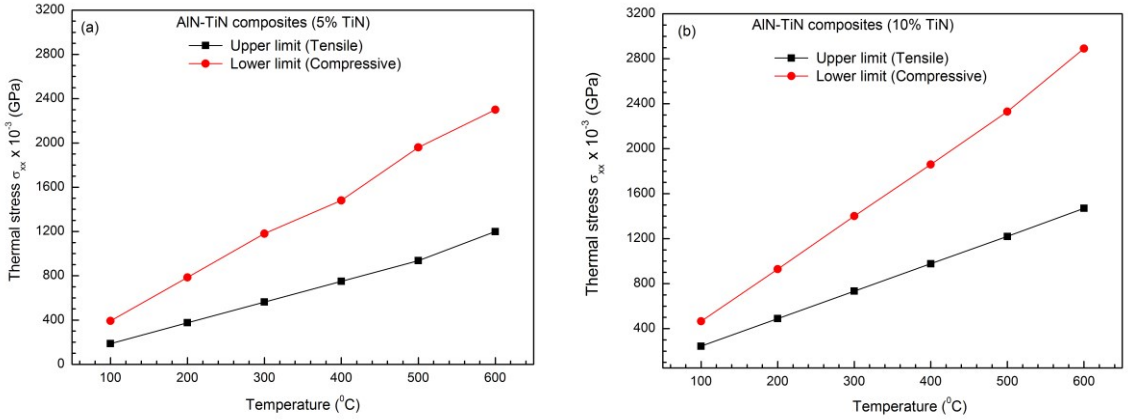

Figure 5:

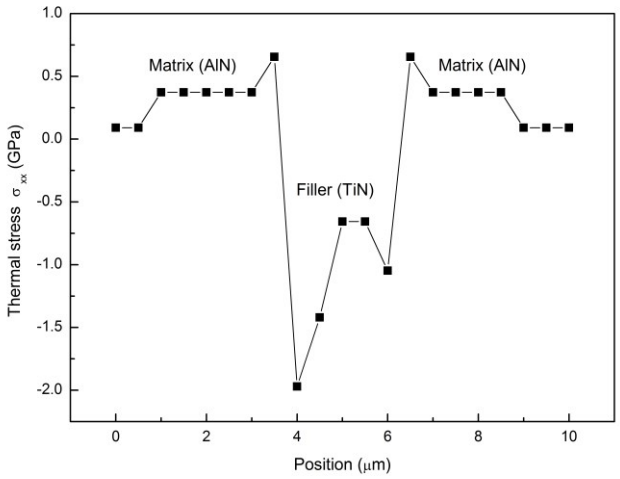

Figure 6 :

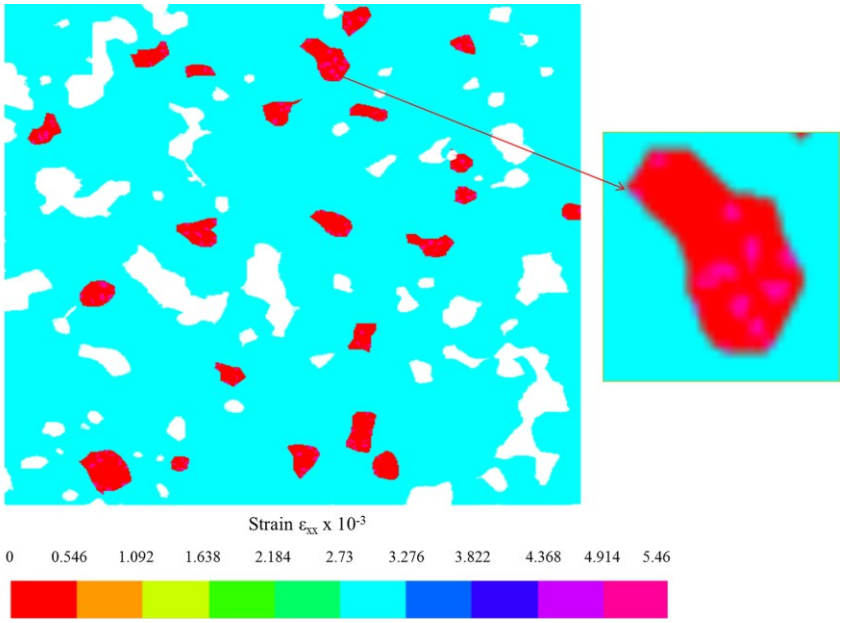

Figure 7:

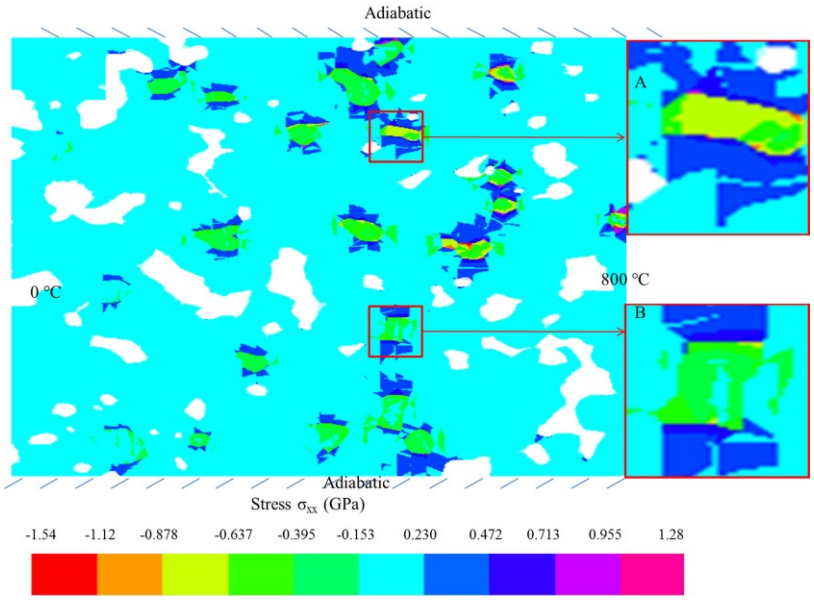

Figure 8:

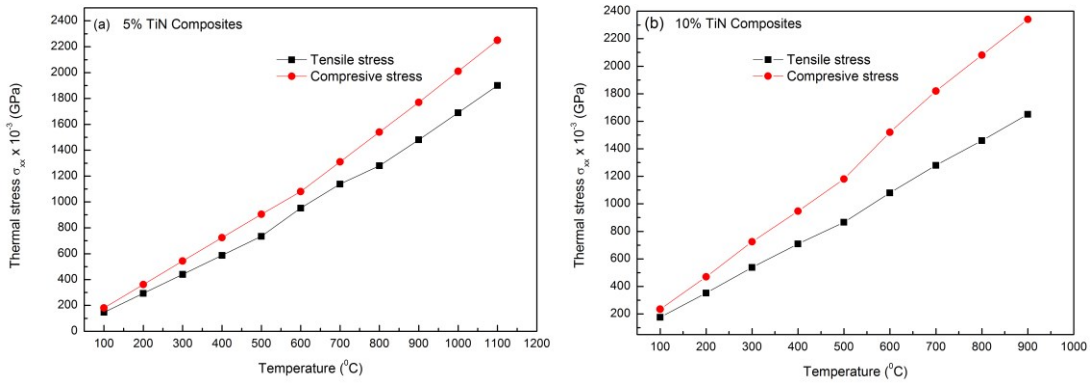

Figure 9:

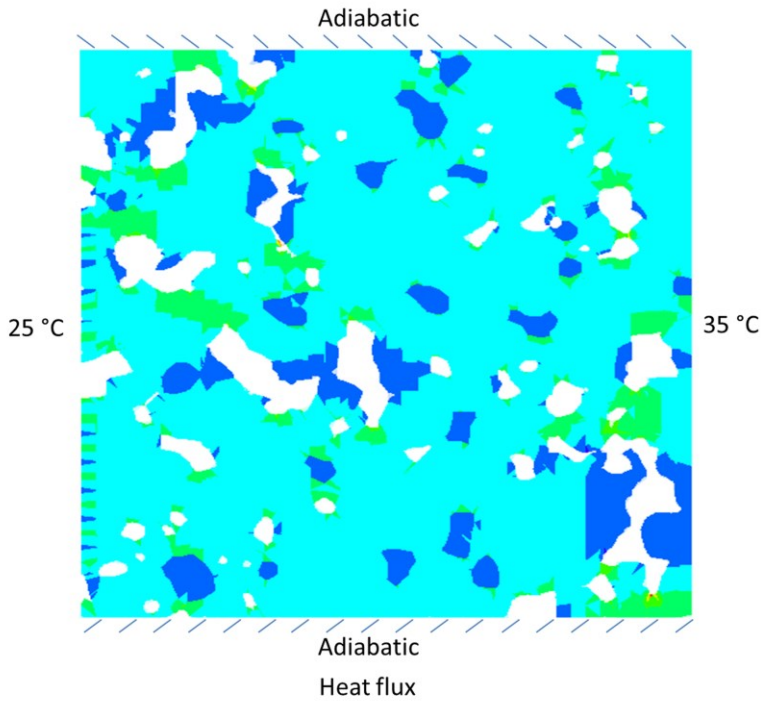

Figure 10:

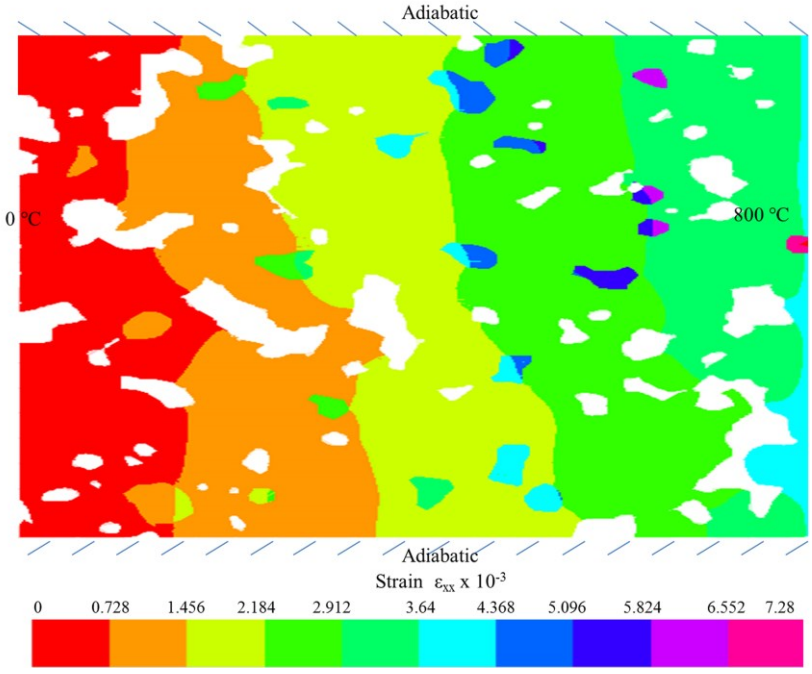

Figure 11